Strathprints Institutional Repository

RESEARCH ARTICLE

Key Points:
- Artificial ionospheric turbulence in the equatorial region is investigated
- Ordinary mode waves induce Langmuir turbulence
- Langmuir turbulence leads to high-energy tail electrons

Correspondence to:
B. Eliasson,
bengt.eliasson@strath.ac.uk

HF wave propagation and induced ionospheric turbulence in the magnetic equatorial region

B. Eliasson[1,2] and K. Papadopoulos[2]

[1]SUPA, Physics Department, University of Strathclyde, Glasgow, UK, [2]Departments of Physics and Astronomy, University of Maryland, College Park, Maryland, USA

Abstract The propagation and excitation of artificial ionospheric turbulence in the magnetic equatorial region by high-frequency electromagnetic (EM) waves injected into the overhead ionospheric layer is examined. EM waves with ordinary (O) mode polarization reach the critical layer only if their incidence angle is within the Spitze cone. Near the critical layer the wave electric field is linearly polarized and directed parallel to the magnetic field lines. For large enough amplitudes, the O mode becomes unstable to the four-wave oscillating two-stream instability and the three-wave parametric decay instability driving large-amplitude Langmuir and ion acoustic waves. The interaction between the induced Langmuir turbulence and electrons located within the 50–100 km wide transmitter heating cone at an altitude of 230 km can potentially accelerate the electrons along the magnetic field to several tens to a few hundreds of eV, far beyond the thresholds for optical emissions and ionization of the neutral gas. It could furthermore result in generation of shear Alfvén waves such as those recently observed in laboratory experiments at the University of California, Los Angeles Large Plasma Device.

1. Introduction

The interaction of large-amplitude high-frequency (HF) radio waves with the ionospheric plasma in the vicinity of the dip equator is significantly different than the well-studied interactions in the polar and middle latitude regions. Previous theoretical study [*Erukhimov et al.*, 1997] proposed a variety of effects including the creation of quasi-periodic structures with vertical periodicity of approximately half the wavelength of the electromagnetic (EM) wave and extending horizontally along the magnetic field lines due to Ohmic heating of the plasma, as well as creation of a virtual antenna at ULF/ELF/VLF frequencies by modulation of the D/E conductivity of the equatorial electrojet similar to the modulation of the polar electrojet in the auroral region [*Rietveld et al.*, 1984, 1987, 1989; *Papadopoulos et al.*, 1990, 2005; *Moore*, 2007; *Payne et al.*, 2007]. Advantages of the equatorial over the polar electrojet modulation were noted by *Papadopoulos et al.* [2005], while *Erukhimov et al.* [1997] emphasized the excitation of low-frequency Alfvén waves in the 1 Hz frequency range. EM waves exceeding a threshold amplitude could also drive artificial ionospheric turbulence (AIT) by the nonlinear interaction of ordinary (O) mode wave with the plasma electrons. In this case, since the O mode has its electric field along the ambient magnetic field lines when it reaches the critical layer, it could excite AIT associated with large amplitude Langmuir waves and ion acoustic waves propagating along the magnetic field. Experiments at the Large Plasma Device (LAPD) at University of California, Los Angeles (UCLA) [*Van Compernolle et al.*, 2006; *Wang et al.*, 2016] have also shown the formation of suprathermal electrons accompanied by the excitation of Alfvén waves when large-amplitude microwaves are injected into the plasma perpendicular to the magnetic field. Particle-in-cell simulations [*Tsung et al.*, 2007] and subsequent laboratory experiments indicate that accelerated electrons due to resonant absorption of the O mode waves, and nonlinear processes involving wave collapse may explain the observation. Ionospheric high-latitude heating experiments at the High-Frequency Active Auroral Program (HAARP) have also demonstrated that AIT correlated with optical emissions and the formation of artificial plasma layers [*Pedersen et al.*, 2009, 2010] can be attributed to high-energy suprathermal electrons accelerated by the turbulence near the O mode critical layer to energies large enough to ionize the neutral gas [*Mishin and Pedersen*, 2011; *Eliasson et al.*, 2012].

The aim of this paper is to investigate the EM wave propagation and generation of AIT in the equatorial region, including resonant acceleration of electrons by the AIT. The manuscript is organized in the following fashion. The basic ionospheric model and parameters are outlined in section 2, where the linear propagation of the O and X modes is investigated with a ray-tracing model. The standing wave pattern, polarization, and swelling of the O mode near the critical layer are studied section 3. In section 4, the growth rate for

Table 1. Ionospheric Parameters

Parameter value	Parameter name
Magnetic field strength	$B_0 = 3.0 \times 10^{-5}$ T
Electron cyclotron frequency	$\omega_{ce} = eB_0/m_e = 5.27 \times 10^6$ s^{-1}
	$f_{ce} = 0.840$ MHz
Transmitted (pump) frequency	$\omega_0 = 50.27 \times 10^6$ s^{-1}
	$f_O = 8.00$ MHz
Vertical thickness of the ionosphere	$L_{n0} = 31.62$ km
F_2 peak density	$n_{0,max} = 8.96 \times 10^{11}$ m^{-3}
F_2 critical frequency	$\omega_{OF2} = 53.41 \times 10^6$ s^{-1}
	$f_{OF2} = 8.50$ MHz
Altitude of F_2 peak	$z_{max} = 300$ km
Critical density at $\omega_0 = \omega_{pe}$	$n_{cr} = 7.94 \times 10^{11}$ m^{-3}
Altitude of critical layer $\omega_0 = \omega_{pe}$	$z_O = 238.99$ km
Altitude of UH layer $\omega_0 = \omega_{UH}$	$z_{UH} = 238.50$ km
Local ionospheric length scale	$L_n = 1/|d\ln n_0/dz|_{z=z_O} = 45.4$ km
Electron temperature	$T_e = 3000$ K
Electron thermal speed	$v_{Te} = \sqrt{k_B T_e/m_e} = 2.13 \times 10^5$ m/s
Ion temperature	$T_i = 1000$ K
Ion acoustic speed (O$^+$ ions)	$C_s = \sqrt{k_B(T_e + 3T_i)/m_i} = 1.76 \times 10^3$ m/s

instabilities driven by the O mode to Langmuir and ion acoustic waves at different altitudes is calculated. The acceleration of electrons by the turbulence is calculated in section 5, and its implications for both ionospheric and laboratory conditions are discussed. Finally, conclusions are drawn in section 6.

2. Ionospheric Model and Ray Tracing

The results of this study are based on the use of an ionospheric model whose parameters are listed in Table 1. For simplicity we use a Gaussian vertical profile of the ionospheric layer of the form $n_0(z) = n_{0,max}\exp\left[-(z - z_{max})^2/L_{n0}^2\right]$, and we adopt a coordinate system such that the horizontal magnetic field $\mathbf{B}_0$ is directed along the x axis.

To lowest order, the propagation of the HF O and extraordinary (X) modes can be estimated using a simple ray-tracing model [e.g., *Whitham*, 1974]

$$\frac{d\mathbf{k}}{dt} = -\nabla\omega \tag{1}$$

$$\frac{d\mathbf{r}}{dt} = \nabla_{\mathbf{k}}\omega \tag{2}$$

where the wave frequency $\omega(\mathbf{k}, \mathbf{r})$ is governed by the Appleton-Hartree dispersion relation based on a cold fluid plasma model [e.g., *Stix*, 1992]

$$\frac{k^2 c^2}{\omega^2} = 1 - \frac{2\omega_{pe}^2\left(\omega^2 - \omega_{pe}^2\right)\omega^{-2}}{2\left(\omega^2 - \omega_{pe}^2\right) - \omega_{ce}^2\sin^2\theta \pm \omega_{ce}\Delta}, \tag{3}$$

where $\Delta = \left[\omega_{ce}^2\sin^4\theta + 4\omega^{-2}\left(\omega^2 - \omega_{pe}^2\right)^2\cos^2\theta\right]^{1/2}$ and θ is the angle between $\mathbf{k}$ and $\mathbf{B}_0$, obtained by the cosine formula $\cos\theta = \mathbf{k}\cdot\mathbf{B}_0/(|\mathbf{k}||\mathbf{B}_0|)$. Here c is the speed of light in vacuum, $\omega_{pe} = \sqrt{n_0 e^2/\epsilon_0 m_e}$ is the electron plasma frequency, and $\omega_{ce} = eB_0/m_e$ is the electron cyclotron frequency, where e is the unit charge, m_e is the electron mass and ϵ_0 is the electric vacuum permittivity. The upper sign (+) is for the O mode and the lower sign (−) is for the X mode. For numerical convenience, equation (3) can be written as

$$\omega^2\left(\omega^2 - \omega_{pe}^2\right)\left(\omega^2 - c^2 k^2 - \omega_{pe}^2\right)^2 - \omega_{ce}^2(\omega^2 - c^2 k^2)\left[\omega^2\left(\omega^2 - c^2 k^2 - \omega_{pe}^2\right) + c^2 k^2\omega_{pe}^2\cos^2\theta\right] = 0. \tag{4}$$

Figures 1 and 2 show a comparison between the propagation of O and X mode waves injected at different angles of incidence for $\omega = \omega_0$. The O mode is converted to Z mode (slow X mode) waves at two angles of incidence, $\chi = \pm\chi_S$, where the Spitze angle for a horizontal magnetic field ($\alpha = 90°$) is given by [*Mjølhus*, 1990]

$$\chi_S = \arcsin\left(\sqrt{\frac{Y}{1 + Y}}\sin\alpha\right) = 17.95°, \tag{5}$$
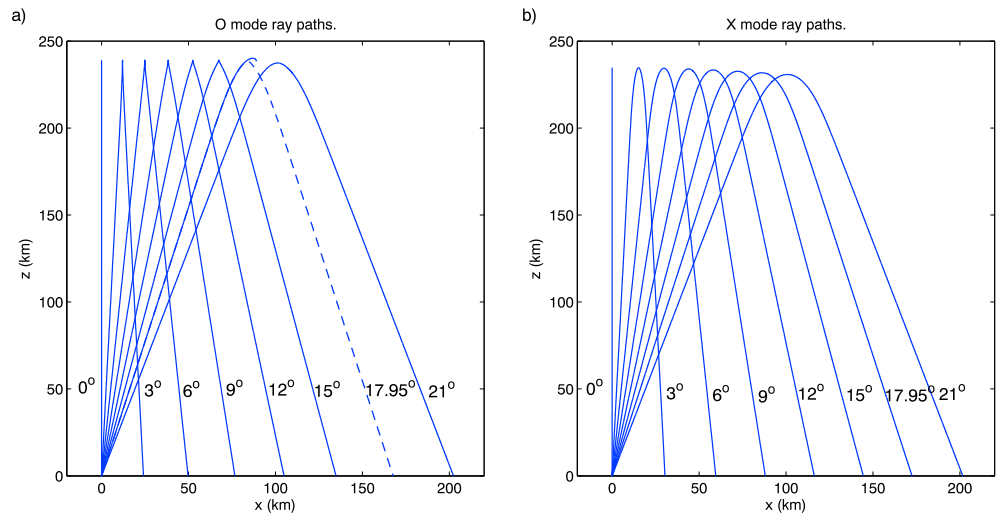
Figure 1. (a) Ordinary (O) mode and (b) fast extraordinary (X) mode waves transmitted at frequency $\omega_0 = 50.27 \times 10^6 \mathrm{s}^{-1}$ (8 MHz) and different angles of incidence χ. The Spitze angle is 17.95°.

and where $Y = \omega_{ce}/\omega_0$. Within the Spitze cone, $|\chi| < \chi_S$, the O mode wave reaches the critical altitude where $\omega = \omega_{pe}$, where there is a strong interaction between the EM wave and electrostatic Langmuir waves propagating along the magnetic field. Since $Y^2 \approx 0.011 \ll 1$, the upper hybrid (UH) layer z_{UH} is only $\approx L_n Y^2 \approx 500$ m below the critical layer z_O (cf. Figure 2 and Table 1). However, since the wave electric field of the O mode is almost parallel to the ambient magnetic field for incidence angles within the Spitze cone, the coupling to UH and lower hybrid waves is expected to be less important. The fast X mode wave is reflected at an altitude about 5 km below the critical layer, and therefore, its coupling to electrostatic waves is expected to be weak.
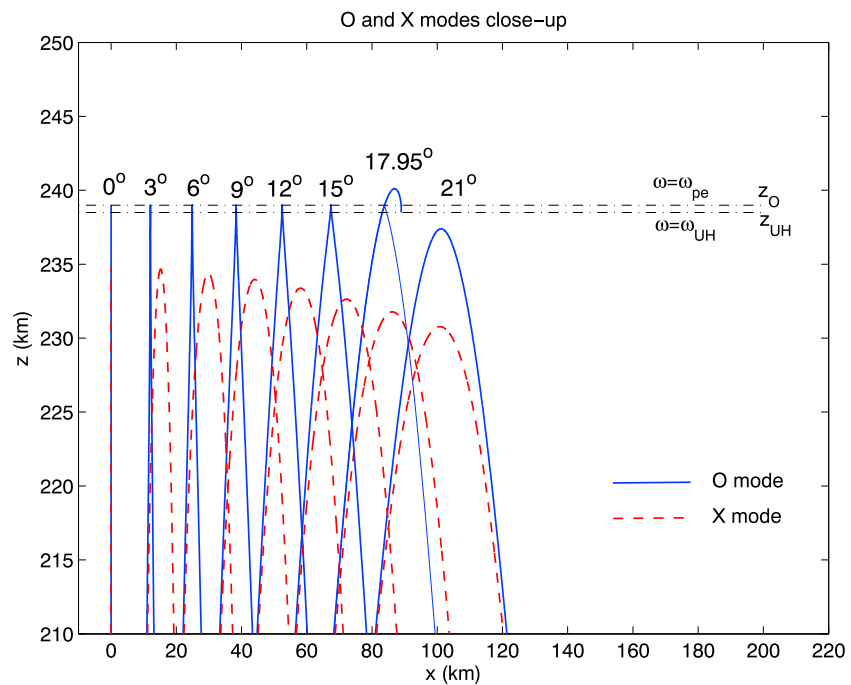

Figure 2. Close-up of the rays of the O and X mode waves (cf. Figure 1) near their turning points. The locations of the critical layer $z_O = 238.99$ km where $\omega = \omega_{pe}$ and UH layer $z_{UH} = 238.50$ km where $\omega = \omega_{UH}$ are indicated with horizontal dash-dotted lines. The Spitze angle is $\chi_S = 17.95°$.
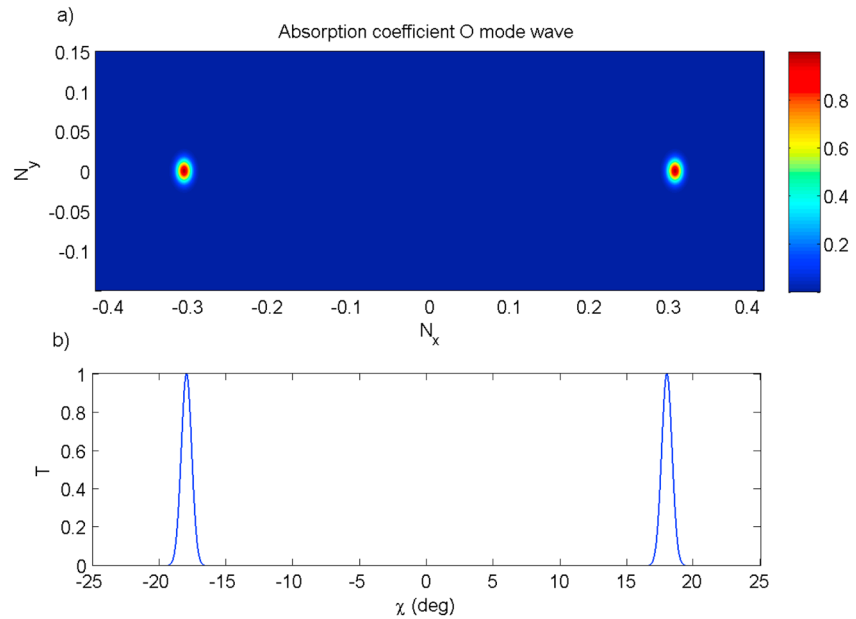
Figure 3. (a) Absorption coefficient for the O mode as a function of the normalized wave vector components N_x and N_y, and (b) of the incidence angle χ at $\phi = 0$. The absorption is significant for angles of incidence only within a few degrees near the Spitze angle $\chi_S = 17.95°$ at $\phi = 0$.

Figure 3 shows the absorption coefficient (absorbed intensity divided by incident intensity) given in equation (18) of *Mjølhus* [1990]. The normalized (by ω_0/c) components of the wave vector of the O mode are $N_x = \sin \chi \cos \phi$ and $N_y = \sin \chi \sin \phi$. The O mode is efficiently absorbed only in a narrow region (the radio window) within 1 or 3 degrees around the Spitze angle $\chi = \chi_S = 17.95°$ and $\phi = 0$, where the O mode is converted to Z mode waves. As seen in the close-up in Figure 2, the mode converted Z mode wave propagates up to an altitude about 1 km above the critical layer of the O mode wave, after which it turns and propagates down to the electrostatic resonance at the UH layer. Outside the Spitze region (e.g., for 21° in Figure 2), the O mode is reflected below the critical layer.

3. Standing Wave Pattern and Swelling Near the O Mode Turning Point

To investigate the standing wave pattern and swelling of an O mode wave near its turning point, we carry out full-wave simulations for different angles of incidence using the model of *Eliasson et al.* [2015], with a linearly polarized (in the *x-z* plane) EM wave injected from the bottom side at $z = 200$ km with a reference amplitude of 1 V/m. A finite electron temperature of 3000 K is used, which has significance only for short wavelength electrostatic waves. As the EM wave reaches the turning point within the Spitze region, there is a swelling of the *x* component of the electric field, and a steady state Airy pattern of the standing wave is formed at time $t = 1$ ms, as seen in Figure 4. The wave amplitude at the first Airy maximum is about 5–8 times larger than the injected amplitude. On the other hand, both the *y* and *z* components (not shown here) are only weakly excited within the Spitze cone. Hence, it is expected that the main nonlinear interaction in this region is Langmuir turbulence due to the coupling of the O mode wave to Langmuir and ion acoustic waves propagating along the magnetic field lines, while the coupling to UH and lower hybrid waves propagating across the magnetic field lines is likely to be less significant.

At the Spitze angle $\chi = \chi_S = 17.95°$ (Figure 4) there are large amplitude mode-converted Z mode waves reaching an altitude of 240 km, about 1 km above the critical layer of the O mode wave. This is consistent with the ray-tracing results in Figure 2. As the Z mode wave is reflected and propagates downwards, it turns into a short wavelength electrostatic UH wave as it passes the UH resonance layer z_{UH} where $\omega_0 = \omega_{UH}$. Large amplitude vertical (*z*) component of the electric field (not shown) for $\chi = 17.95°$ could potentially lead to nonlinear excitations of UH and lower hybrid turbulence in a small region (cf. Figure 3) near the Spitze angle.
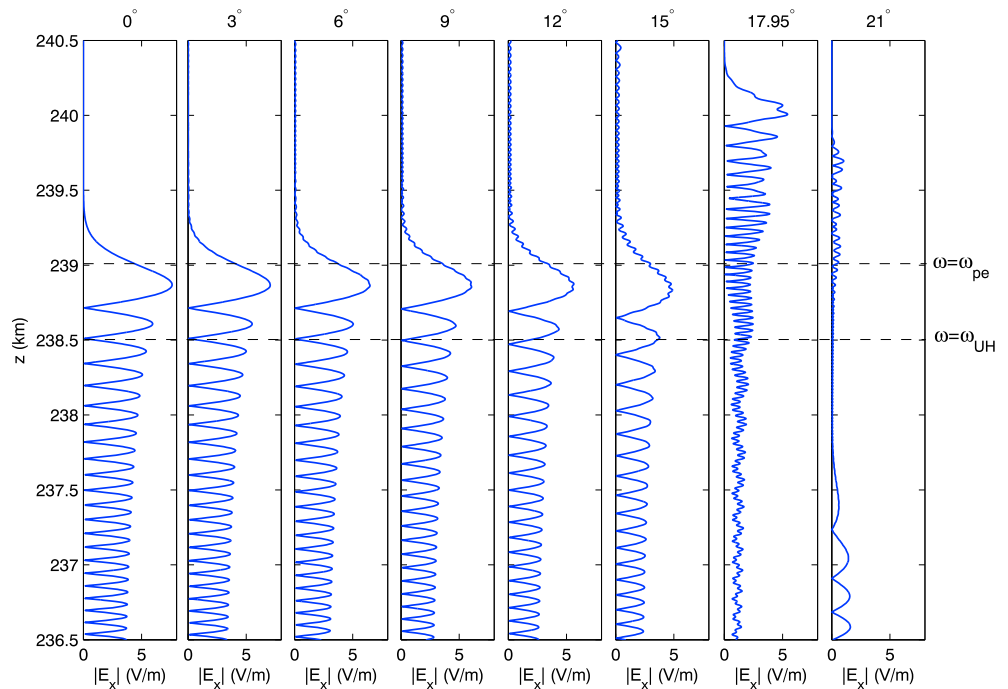
Figure 4. Standing wave pattern of the horizontal x component (parallel to the magnetic field) of the EM wave electric field near the O mode cutoff at $t = 1$ ms. At the Spitze angle $\chi_S = 17.95°$ there is significant mode conversion to Z mode waves propagating to about 240 km after which they turn downwards and are converted to electrostatic UH waves.

4. Threshold for Artificial Ionospheric Turbulence

A vertically (along z) injected O mode wave has the wave electric field parallel to the ambient magnetic field in the x direction. Above a threshold amplitude, the O mode will be unstable and decay to high-frequency Langmuir waves and low-frequency ion density fluctuations. The swelling of the EM wave seen in Figure 4 near the O mode turning point significantly boosts the nonlinearity. In general, the four-wave oscillating two-stream instability (OTSI) dominates at higher altitudes near the critical layer, while at lower altitudes the three-wave parametric decay instability (PDI) dominates [e.g. *Mjølhus et al.*, 1995]. Figure 5 shows a schematic of the two processes. The OTSI excites nonresonant, purely growing ion density fluctuations and saturates nonlinearly by strong turbulence associated with wave localization and collapse (nucleation and burnout cycles) [e.g., *Russell et al.*, 1988], while the PDI excites resonant Langmuir and ion acoustic waves associated with weak turbulence where the involved waves approximately obey the respective linear dispersion relations.
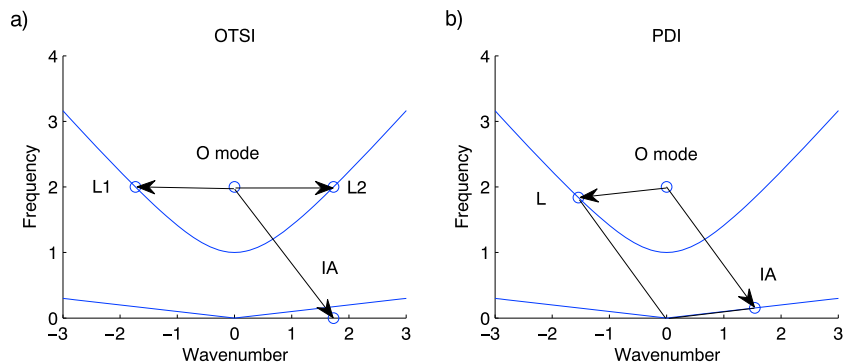

Figure 5. (a) The four-wave OTSI with the O mode decaying into two Langmuir waves (L1 and L2) and nonresonant purely growing ion mode and (b) the three-wave PDI with the O mode decaying to resonant Langmuir (L) and ion acoustic (IA) waves. (The axes are in arbitrary units and scales have been enhanced for clarity.)
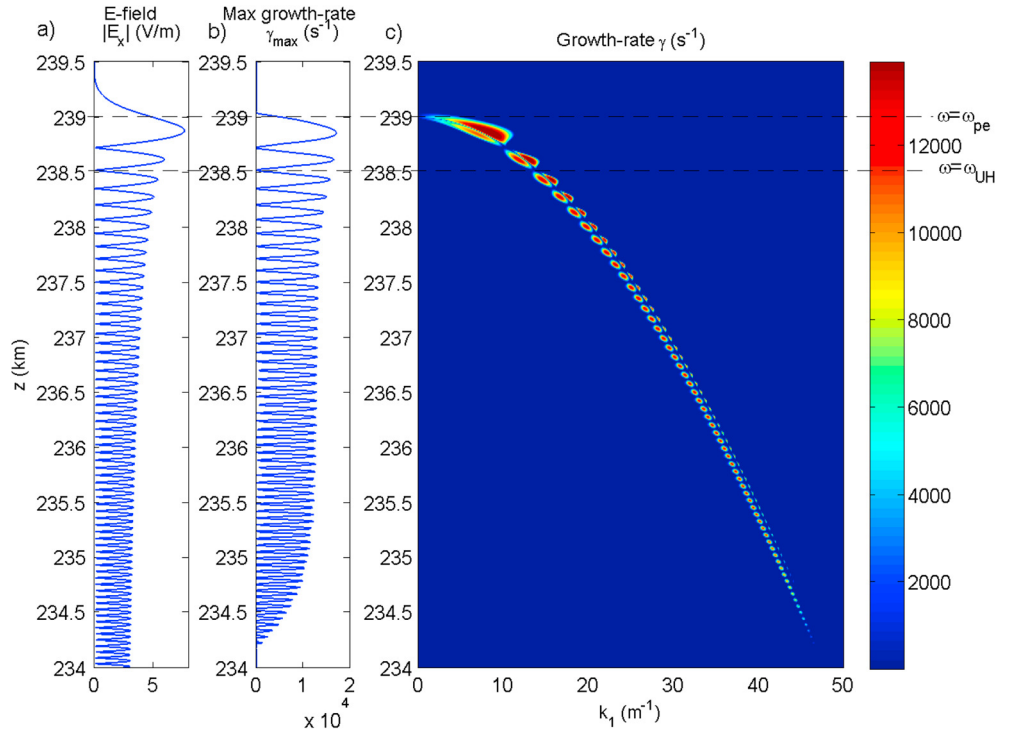
Figure 6. (a) The amplitude of the vertically injected O mode wave with amplitude $E_{EM} = 1$ V/m. (b) The maximum growth rate of the instability and (c) the growth rate as a function of perturbation wave number at different altitudes. No significant instability takes place above the critical layer where $\omega = \omega_{pe}$, and the instability region is terminated about 5 km below the critical layer due to the strong electron Landau damping at large wave numbers.

The growth rates of the PDI and OTSI can be obtained from a model involving large amplitude electric field oscillations coupled with low-frequency ion fluctuations via the ponderomotive force acting on the electrons [e.g., *Papadopoulos et al.*, 1974; *Freund and Papadopoulos*, 1980]. Parallel to the magnetic field, the dispersion relation for the growth rate of the instability is (see details in Appendix A)

$$-\omega_1^2 - 2i\nu_i\omega_1 + C_s^2 k_1^2 = \frac{\epsilon_0 E_0^2 \omega_{pe}^2 k_1^2}{4m_i n_0}\left(\frac{1}{D_+} + \frac{1}{D_-}\right), \tag{6}$$

where $D_\pm = -(\pm\omega_0 + \omega_1)^2 + i\nu_e(\pm\omega_0 + \omega_1) + 3\nu_{Te}^2 k_1^2 + \omega_{pe}^2$ represent the sidebands of the Langmuir wave and E_0 is the local amplitude of the O mode pump electric field. The perturbation wave number and frequency is denoted k_1 and $\omega_1 = \omega_R + i\gamma$, respectively, where ω_R is the real frequency and γ is the growth rate. Here $\nu_{Te} = \sqrt{k_B T_e/m_e}$ is the electron thermal speed and $C_s = \sqrt{k_B(T_e + 3T_i)/m_i}$ is the ion acoustic speed, where m_i is the ion mass (we use atomic oxygen ions) and k_B is Boltzmann's constant. Near the critical layer, where $\omega_0 \approx \omega_{pe}$, the OTSI dominates, while the PDI dominates at lower altitudes where the frequency mismatch $\Delta\omega = \omega_0 - \omega_{pe}$ is larger.

In equation (6), $\nu_e = \nu_{ei} + \nu_{eL}$ and $\nu_i = \nu_{iL}$ are electron and ion damping rates due to collisions and Landau damping. The electron-ion collision frequency due to Coulomb collisions may be estimated by $\nu_{ei} \approx 0.25\omega_{pe}\log(\Lambda)/\Lambda$, where $\Lambda = 4\pi n_0\lambda_{De}^3$ is the plasma parameter. In the numerical work below, we use $\nu_{ei} = 10^3 s^{-1}$, which is consistent with the ionospheric parameters in Table 1. The relative importance of collisions increases with density, which has to be taken into account when comparing ionospheric and laboratory experiments. The electron and ion Landau damping rates are approximated by [e.g., *Krall and Trivelpiece*, 1986]

$$\nu_{eL} = \sqrt{\frac{\pi}{8}}\frac{\omega_{pe}}{|k_1\lambda_{De}|^3}\exp\left[-\frac{1}{2(k_1\lambda_{De})^2}\right] \tag{7}$$
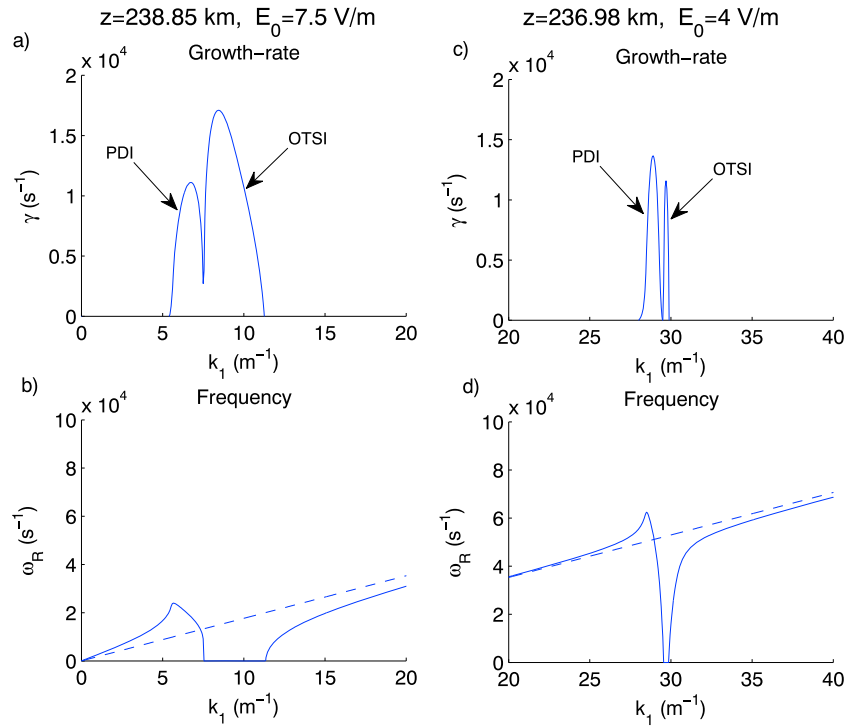
Figure 7. Line plots of the (a and c) growth rate and (b and d) real frequency of the PDI and OTSI for an injected O mode amplitude of 1 V/m. The line plots are taken for two altitudes: (Figures 7a and 7b) $z = 238.85$ km where the local O mode electric field is $E_0 = 7.5$ V/m (cf. Figure 6a) and the frequency mismatch $\Delta\omega = \omega_0 - \omega_{pe} = 7.7 \times 10^3 \mathrm{s}^{-1}$ (1.2 kHz) and (Figures 7c and 7d) $z = 236.98$ km where $E_0 = 4$ V/m and $\Delta\omega = 1.2 \times 10^6 \mathrm{s}^{-1}$ (190 kHz). The unperturbed ion acoustic frequency $\omega_1 = C_s k_1$ is indicated with dashed lines in Figures 7b and 7d. The PDI gives ion acoustic waves near the ion acoustic frequency, while the OTSI is purely growing.

and

$$v_{iL} = \sqrt{\frac{\pi}{8}} C_s |k_1| R^{3/2} \exp\left(-\frac{3+R}{2}\right) \tag{8}$$

where $R = T_e/T_i$ is the electron-to-ion temperature ratio and $\lambda_{De} = v_{Te}/\omega_{pe}$ is the electron Debye length. The used $T_e = 3000$ K and $T_i = 1000$ K gives significant ion Landau damping. Electron Landau damping of Langmuir waves becomes significant when $k_1 \lambda_{De} \gtrsim 0.2$, which for our parameters (with $\lambda_{De} \approx 4$ mm) is for wave numbers $k_1 \gtrsim 50$ m^{-1} corresponding to wavelengths smaller than about 13 cm.

On longer length scale and time scale, the coupling to collisional modes and the plasma drift due to gradients [*Stenflo*, 1985] may become important for the formation of quasi-periodic structures in the vertical direction [e.g., *Erukhimov et al.*, 1997] and other temperature-driven effects. However, while thermal instabilities in ionospheric heating experiments may develop on time scales of the order of a second [e.g., *Gurevich*, 1978], Langmuir turbulence usually develops on millisecond time scales. We therefore neglect the effect of plasma temperature changes in the present treatment.

Figures 6–9 show numerical solutions of equation (6) as a function of perturbation wave number at different altitudes, where estimates of the O mode pump electric field $E_0 = |E_x|$ at different altitudes are taken from the standing wave pattern for vertical incidence (i.e., for 0° in Figure 4). Since the length scale of the O mode wave is about 2–3 orders of magnitude larger than that of the Langmuir waves, we assume that E_0 (as well as n_0) is locally independent of space in the numerical solution of equation (6). As seen in Figures 6 and 8, the instability takes place in a quasi-periodic pattern with maximum growth rate at the Airy maxima of the O mode wave. Figures 6 and 7 show the growth rate of the instabilities for an injected O mode amplitude of $E_{EM} = 1$ V/m. It is seen in Figures 6b and 6c that the instability takes place in a region covering about 4–5 km below the critical layer. This is in contrast to the high-latitude cases [e.g., *Eliasson and Stenflo*, 2008; *Eliasson et al.*, 2012, 2015], where the region of Langmuir turbulence covers only a fraction of a kilometer.
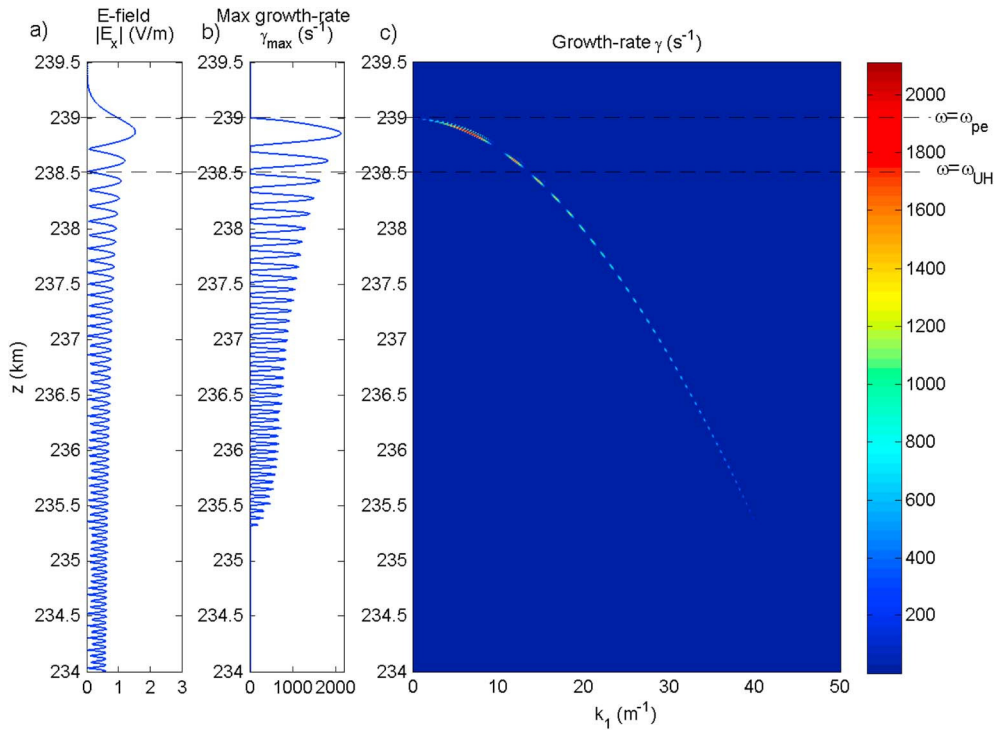
Figure 8. Same as Figure 6 for injected O mode amplitude $E_{EM} = 0.2$ V/m. The instability region is terminated about 3.5 km below the critical layer due to the onset of strong electron Landau damping at large wave numbers.
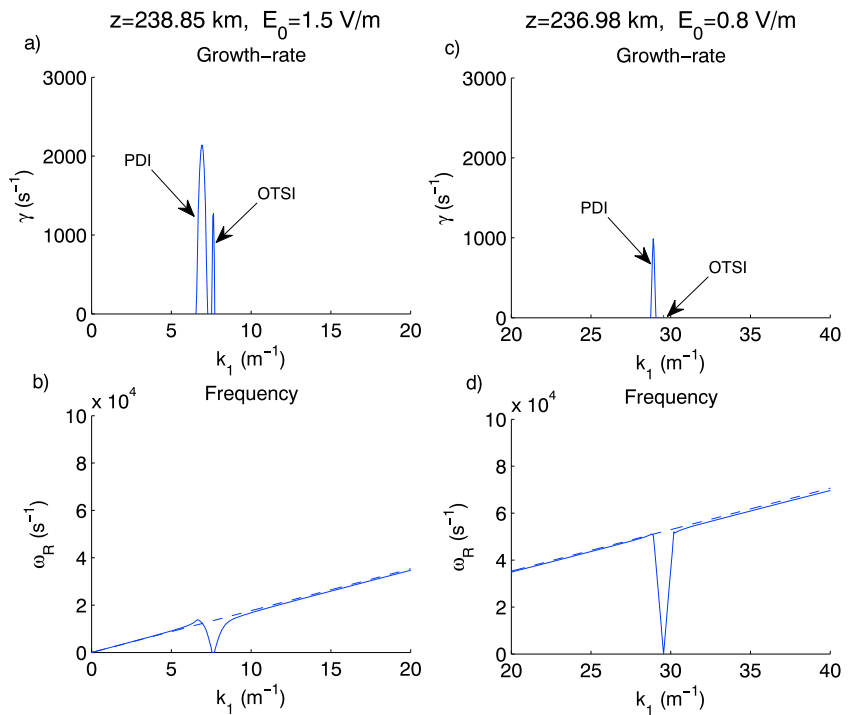
Figure 9. Same as Figure 7 for an injected O mode amplitude of 0.2 V/m. The line plots are taken for two altitudes: (a and b) $z = 238.85$ km where the local O mode electric field is $E_0 = 1.5$ V/m (cf. Figure 8a) and $\Delta\omega = 7.7 \times 10^3 \text{s}^{-1}$ (1.2 kHz) and (c and d) $z = 236.98$ km where $E_0 = 0.8$ V/m and $\Delta\omega = 1.2 \times 10^6 \text{s}^{-1}$ (190 kHz). The unperturbed ion acoustic frequency $\omega_1 = C_s k_1$ is indicated with dashed lines in Figures 9b and 9d.

Figure 10. Results from 2-D Zakharov simulations for a large-amplitude injected O mode with $E_{EM} = 1$ V/m (cf. Figures 6 and 7). (a–c) The electric field and ion density fluctuations at $t = 5$ ms at the first Airy maximum at $z = 238.85$ km where $E_0 = 7.5$ V/m and (d and e) at about 2 km lower altitude $z = 236.98$ km where $E_0 = 4$ V/m.

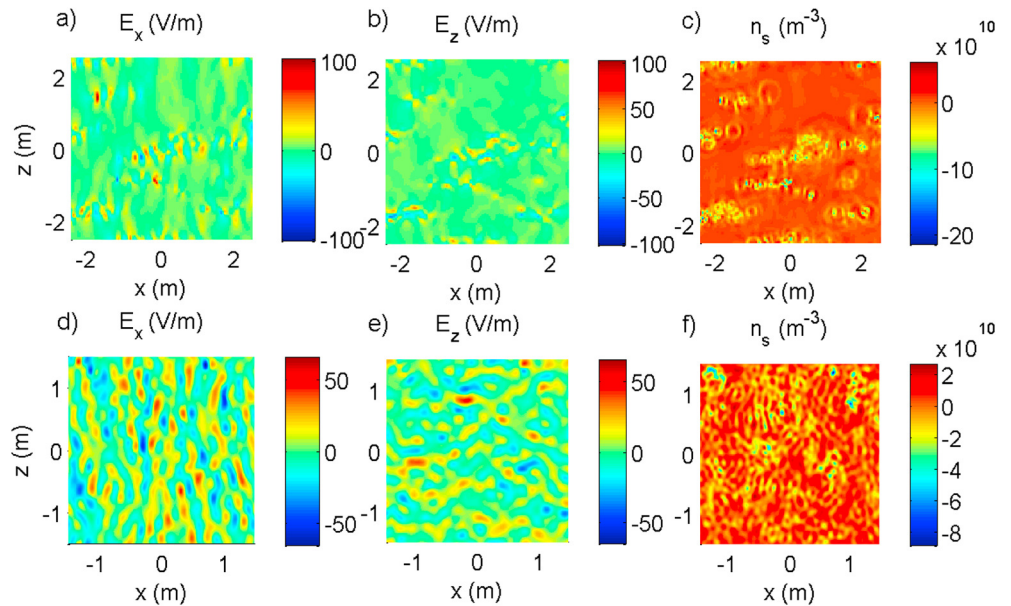With a growth rate of the order 10^4 s^{-1} (cf. Figure 6b) the instability will typically saturate nonlinearly within a few milliseconds after switch on of the heating. Near the critical layer, the instability gives rise to Langmuir waves and ion density fluctuations at wave number of the order $k_1 \sim 5$–15 m^{-1} (cf. Figure 6c) corresponding to wavelengths of the order 0.5–1 m, while at lower altitudes the instability takes place for larger wave numbers (shorter wavelengths) of the generated waves. The electron Landau damping becomes strong enough to quench the instability about 4.5 km below the critical layer, where the wave number of the Langmuir waves is sufficiently large, $k_1 \approx 45$ m^{-1} (cf. Figure 6c) corresponding to a wavelength of about 15 cm.

The line plots in Figure 7 show that the OTSI has a higher the growth rate than the PDI at the first Airy maximum ($z = 238.85$ km) where the frequency mismatch $\Delta\omega = \omega_0 - \omega_{pe} = 7.7 \times 10^3$ s^{-1} (1.2 kHz), while the PDI has a larger growth rate at the lower altitude 2 km below the critical layer ($z = 236.98$ km) where $\Delta\omega = 1.2 \times 10^6$ s^{-1} (190 kHz). While the OTSI gives rise to purely growing ion fluctuations (cf. Figure 7b), the PDI is an oscillating instability giving rise to ion acoustic waves with frequencies near the unperturbed ion acoustic frequency.

While the relatively large injected O mode amplitude of $E_{EM} = 1$ V/m is believed to be typical for large facilities such as HAARP with access to large transmitted powers and antenna gains, such high amplitudes may be out of reach for proposed [*Papadopoulos*, 2015] portable heating facilities in the equatorial region. It is therefore of interest to investigate a case of significantly lower amplitude. As an example, we take an injected amplitude of 0.2 V/m, corresponding to a factor 25 smaller power than for 1 V/m. Most importantly, it is seen in Figure 8 that the excitation of AIT is still possible at this relatively low O mode amplitude. This is due to the swelling of the injected O mode near the critical layer with a local increase of the amplitude by a factor 5–8 compared to the free space amplitude, above the threshold for instability. The instability takes place in a somewhat smaller, 3.5 km wide region, and with an order of magnitude smaller growth rate. For this case, the PDI has in general a larger growth rate than the OTSI (Figure 9), and the OTSI quickly vanishes at lower altitudes (cf. Figure 9c).

5. Nonlinear Evolution and Formation of Suprathermal Electrons

To study the turbulence induced by the large amplitude EM wave and the resulting electron acceleration, we carry out local simulations using a two-dimensional (2-D) generalized Zakharov model in the *x-z* plane, in which the envelope of the HF electrostatic waves is nonlinearly coupled to the slowly varying ion density fluctuations via the ponderomotive force acting on the electrons. Such local turbulence simulations have
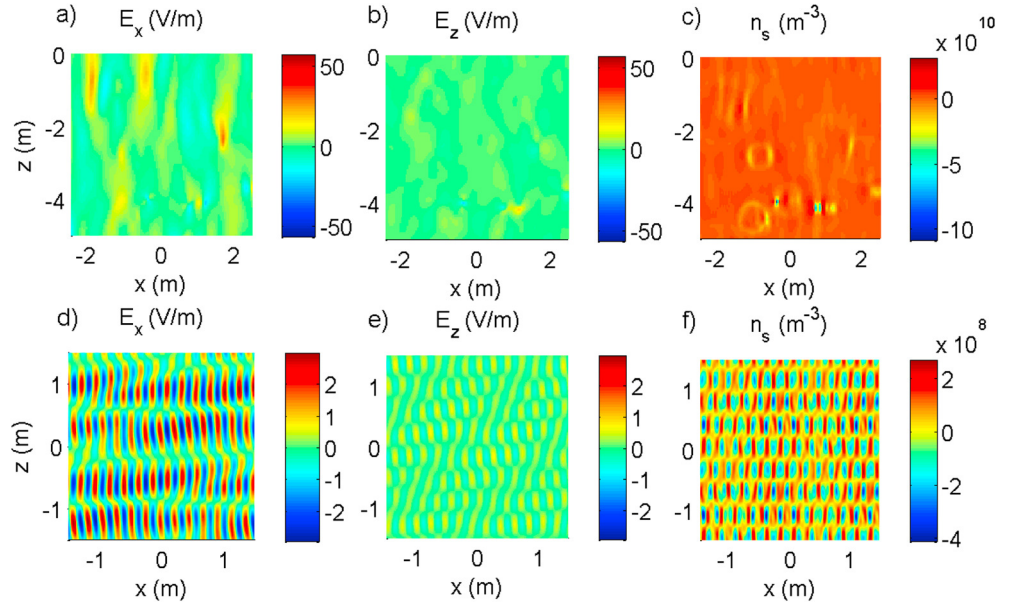
Figure 11. Results from 2-D Zakharov simulations for a small-amplitude injected O mode with $E_{EM} = 0.2$ V/m (cf. Figures 8 and 9). (a–c) The electric field and density fluctuation at $t = 10$ ms at the first Airy maximum at $z = 238.85$ km where the local amplitude is $E_0 = 1.5$ V/m and (d and e) at $t = 30$ ms at about 2 km lower altitude $z = 236.98$ km where $E_0 = 0.8$ V/m.

previously been used to study turbulence and stimulated EM emissions from unmagnetized and magnetized plasma [*Mjølhus et al.*, 1995, 2003]. The electron continuity and momentum equations of motion for the complex valued envelopes of the high-frequency electron density and velocity are

$$\frac{\partial n_e}{\partial t} = i\omega_0 n_e - \nabla \cdot (n_s \mathbf{v}_e) \tag{9}$$

and

$$\frac{\partial \mathbf{v}_e}{\partial t} = i\omega_0 \mathbf{v}_e - \frac{e}{m_e}(-\nabla\phi + \mathbf{E}_0 + \mathbf{v}_e \times \mathbf{B}_0) - \frac{3v_{Te}^2}{n_0}\nabla n_e - v_e\mathbf{v}_e \;, \tag{10}$$

respectively, where $\mathbf{B}_0 = B_0\hat{\mathbf{x}}$. The envelope of the HF electrostatic potential, ϕ, is obtained from Poisson's equation

$$\nabla^2\phi = \frac{e}{\epsilon_0}n_e. \tag{11}$$

The external electric field $\mathbf{E}_0 = E_0\hat{\mathbf{x}}$ is a dipole field (constant in space) along the *x* axis, representing the O mode wave, where we will use the values of E_0 discussed in Figures 7 and 9. The influence of the low-frequency fluctuations on the high-frequency dynamics is through the slow time scale electron and ion density $n_{es} = n_{is} = n_s$ in equation (9). The low-frequency ion motion is governed by the ion continuity and momentum equations

$$\frac{\partial n_s}{\partial t} = -n_0\nabla \cdot \mathbf{v}_s \tag{12}$$

and

$$\frac{\partial \mathbf{v}_s}{\partial t} = -\frac{C_s^2}{n_0}\nabla n_s - \frac{\epsilon_0}{4n_0 m_i}\frac{\omega_{pe}^2}{\omega_0^2}\nabla|\mathbf{E} + \mathbf{E}_0|^2 - 2v_i\mathbf{v}_s \;, \tag{13}$$

where the second term on the right-hand side is due to the ponderomotive force acting on the electrons [see, e.g., *Thornhill and Ter Haar*, 1978]. At equilibrium, $n_s = n_0$, where n_0 is the local density given by the altitude-dependent ionospheric profile.

Figures 10 and 11 show numerical solutions of equations (9)–(13) for the large and small amplitude of the pump electric field used in Figures 7 and 9, respectively. The spatial derivatives as well as the Landau damping

effects are accurately approximated in the simulations using pseudo spectral methods, in which the formulas (7) and (8) are used to calculate electron and ion Landau damping in Fourier space [cf. *Mjølhus et al.*, 2003]. The quadratic nonlinearities are dealiased using a two-third rule based on zero padding in Fourier space before multiplication [e.g., *Gumerov et al.*, 2011]. A two-dimensional domain is used, resolved by 250 grid points with periodic boundary conditions in both the x and z direction. The domain size is taken to be 10×10 m in Figures 10a–10c and 11a–11c and 3×3 m in Figures 10d–10f and 11d–11f to accurately resolve the turbulence. A standard fourth-order Runge-Kutta scheme is used to advance the solution in time, with a time step $\Delta t = 10^{-8} \text{s}^{-1}$. Small-amplitude density perturbations (random numbers) of the order 10^7m^{-3} are added to n_e to seed the instability. The instability in general first develops with electrostatic waves along the magnetic field lines, consistent with equation (6). After the initial nonlinear one-dimensional saturation, the turbulence in some cases enters a second phase of OTSI-generated 2-D nucleation and burnout cycles similar to that discussed by *Russell et al.* [1988] and others. The simulations initially show exponential growth of the PDI and OTSI instabilities in time, after which a transition to steady state turbulence takes place. The results in Figures 10 and 11 are recorded when the turbulence has reached steady state.

For the large amplitude injected O mode, the OTSI at the higher altitude at first Airy maximum of the O mode wave (cf. Figure 10a–10c) leads to turbulence characterized by nucleation and burnout cycles [cf. *Russell et al.*, 1988], in which large amplitude localized electric fields self-trapped in ion density cavities collapse and dissipate. At the lower altitude (cf. Figure 10d–10f), the PDI leads to the excitation of propagating ion acoustic waves, in addition to the OTSI-generated nucleation and burnout cycles.

For the smaller injected O mode amplitude $E_{EM} = 0.2$ V/m is shown in Figure 11. The turbulence near the first Airy maximum, shown in Figures 11a–11c, is characterized by PDI-generated wave turbulence together with only a few nucleation and burnout events due to the OTSI, giving rise to transient large-amplitude electric fields correlated with ion cavities. In this process, ion acoustic waves are excited and propagate away radially giving rise to a few circular patterns visible in Figure 11c. At the lower altitude, displayed in Figures 11d–11f, the instability is dominated by the PDI, while the OTSI is absent (cf. Figure 9d), and the nonlinear saturation is characterized by weak turbulence involving propagating Langmuir and ion acoustic waves, but no nucleation and burnout events are visible.

The x components of the HF electric fields in Figures 10 and 11 are used to estimate the acceleration and transport of electrons along the magnetic field lines by the turbulent electric field. When the electrons have sufficiently high velocities, they feel an almost constant electric field when they pass over localized electric field envelopes. This leads to a random walk process and a diffusion of the electron distribution in velocity space. As a crude approximation, this process is modeled by a one-dimensional Fokker-Planck equation for the averaged electron distribution [e.g., *Sagdeev and Galeev*, 1969]

$$\frac{\partial F_e}{\partial t} + v_x \frac{\partial F_e}{\partial x} = \frac{\partial}{\partial v_x} D(v_x) \frac{\partial F_e}{\partial v_x} \tag{14}$$

with the diffusion coefficient

$$D(v_x) = \frac{\pi e^2}{m_e^2} \frac{W(\omega_0, \omega_0/v_x)}{|v_x|} \quad , \tag{15}$$

where $W(\omega_0, k_x) = \Delta E_x^2 / \Delta k_x$ is the spectral energy density of the electric field per wave number Δk and ΔE^2 is the differential squared electric field. Here W is in V^2/m and is normalized such that the total spectral energy equals the mean squared electric field

$$\int W(\omega, k_x) \, dk_x = \frac{1}{L_x} \int_{x_0}^{x_0+L_x} E_x^2 \, dx \quad , \tag{16}$$

where L_x is the width of the turbulent region. Extensions of the model to multiple dimensions leads to a set of integrodifferential equations [e.g., *Vedenov et al.*, 1961; *Ivanov et al.*, 1975]. A convective term has been added to the left-hand side of equation (14) to account for the transport of electrons through a turbulent layer of finite width. To numerically construct the diffusion coefficient (15), the energy spectrum of E_x is calculated along the x direction and is averaged in the y direction over the simulation domain. An average is also taken over 10 different times covering 10^{-4} s. The resulting diffusion coefficients are shown in Figure 12. They are characterized by a gap at low velocities, and hence, only sufficiently fast electrons are efficiently accelerated by the turbulence to form high-energy tails in the distribution function.
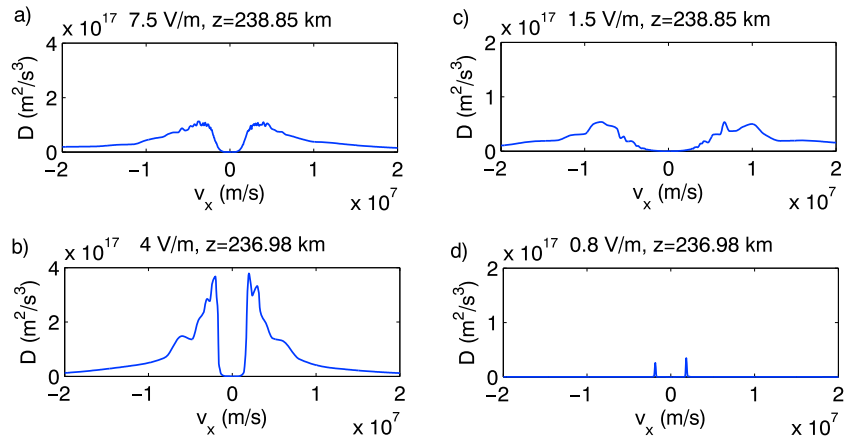
Figure 12. Diffusion coefficients calculated from the E_x data for a (a and b) large-amplitude and (c and d) small-amplitude injected O mode wave, near the first Airy maximum at $z = 238.85$ km (Figures 12a and 12c) and about 2 km lower altitude at $z = 236.98$ km (Figures 12b and 12d).

The diffusion coefficients in Figure 12 are used in a set of Fokker-Planck simulations, shown in Figures 13–15. In the simulations, the boundary condition on the left-hand boundary is to inject a Maxwellian electron velocity distribution with $T_e = 3000$ K for $v_x > 0$ and to use an absorbing boundary condition for $v_x < 0$ and vice versa on the opposite, right-hand boundary. The simulations are run until steady state, after which the results

Figure 13. Electron distribution functions developed at the first Airy maximum at $z = 238.85$ km using a local pump amplitude of 7.5 V/m, assuming (a) a 100 m wide turbulent region and (b) a 1 km wide turbulent region. (c) The velocity distribution of electron streaming out of the turbulent region over the right-hand boundary for the narrow (solid line) and wide (dashed line) region, compared with the unperturbed Maxwellian distribution (dotted line).

Figure 14. Electron distribution functions developed at $z = 236.98$ km using a local pump amplitude of 4 V/m, showing (a) 100 m wide turbulent region and (b) 1 km wide turbulent region. (c) The velocity distribution of electron streaming out of the turbulent region over the right-hand boundary for the narrow (solid line) and wide (dashed line) region, compared with the unperturbed Maxwellian distribution (dotted line).

are recorded. In each set of simulations we consider two widths of the simulation domain. The smaller width of 100 m is approximately three vacuum wavelengths of the O mode wave and corresponds roughly to the width of the spot size in the lab experiment of *Van Compernolle et al.* [2006] where the width of the interaction region of 10 cm is approximately three wavelengths of the 9 GHz microwave. In Figure 13a we see that the electrons passing through this region form significant suprathermal tails with the fastest electrons having a velocity of approximately 0.5×10^7 m/s, corresponding to about 70 eV energy. This is in line with the experiment [*Van Compernolle et al.*, 2006] where the highest energy of the electrons were about 75 eV. For a 10 times wider region shown in Figure 13b, which may be more representative of ionospheric experiments, the highest energy suprathermal electrons reach about 10^7 m/s, corresponding to about 280 eV. The line plots in Figure 13c show the distribution function of the electrons streaming out of the turbulent region for the respective cases. It should be noted that electrons above about 2 eV energy lead to optical emissions by exciting the 1-D state of atomic oxygen, while energies above 12 eV leads to ionization of molecular oxygen [e.g., *Pedersen et al.*, 2009; *Rees*, 1989]. The suprathermal electrons far exceed these thresholds, and hence, both optical emissions and the formation of artificial plasma near the Airy maxima of the O mode wave are expected for this case.

Figure 14 shows simulation results at the lower altitude $z = 236.98$ km, where the local amplitude of the O mode wave is about 4 V/m. Also in this region, the OTSI-generated wave collapse leads to significant acceleration of suprathermal electron tails. For the narrow region (solid line in Figure 14c) a small fraction of electrons also here reaches a velocity of about 0.5×10^7 m/s, corresponding to an energy of about 70 eV, while in the wider region (dashed line) the electron energy reaches about 280 eV.

For the case of a weaker injected O mode amplitude of 0.2 V/m, strong turbulence is observed only at the higher altitude near the first Airy maximum (cf. Figures 11a–11c), and the corresponding diffusion coefficient
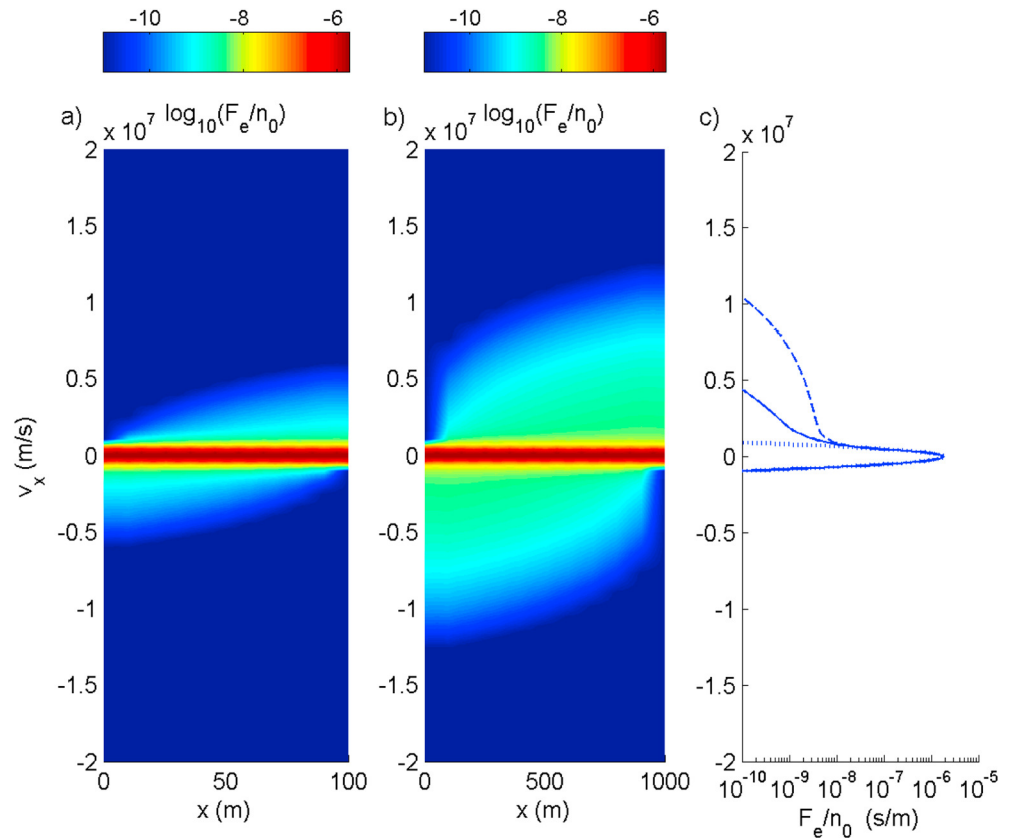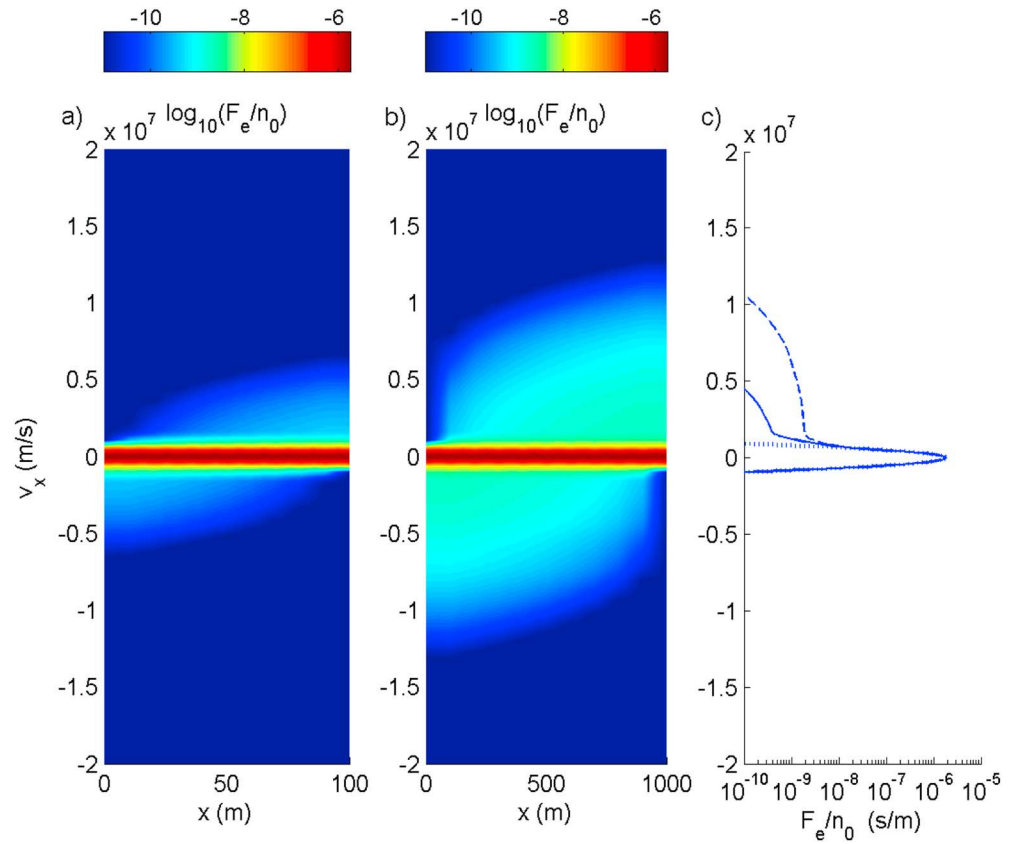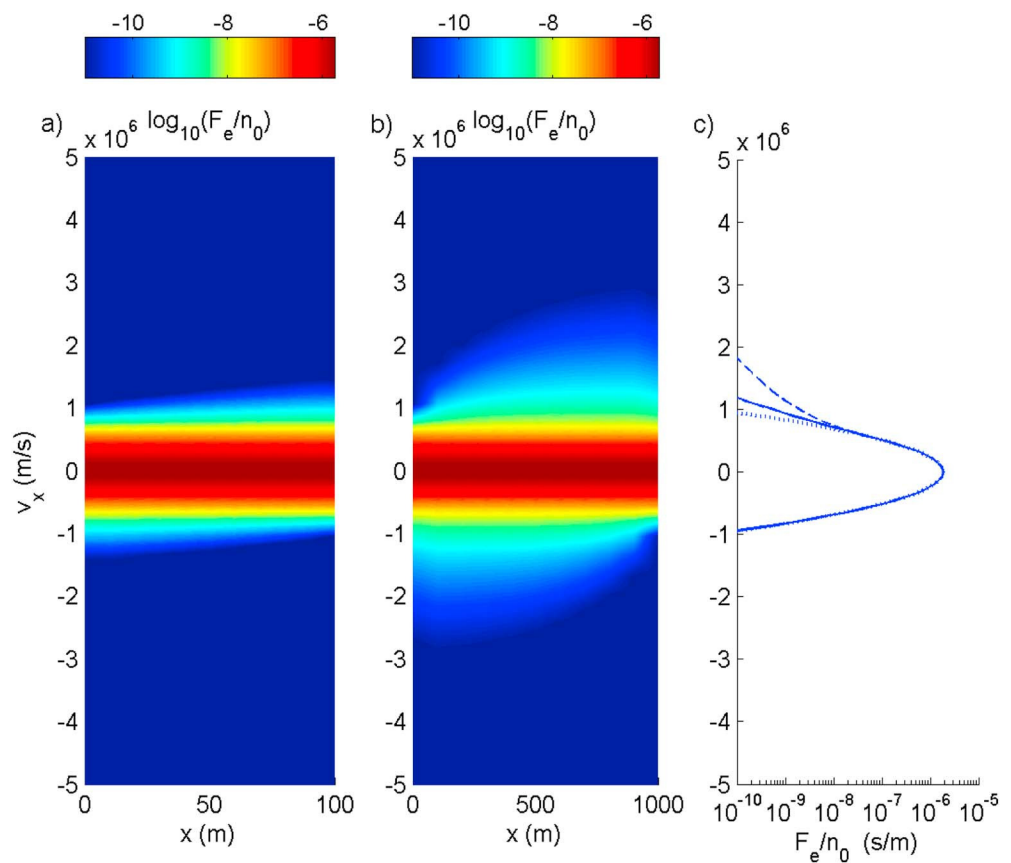
Figure 15. Electron distribution functions developed at the first Airy maximum at $z = 238.85$ km using a local pump amplitude of 1.5 V/m, showing (a) 100 m wide turbulent region and (b) 1 km wide turbulent region. (c) The velocity distribution of electron streaming out of the turbulent region over the right-hand boundary for the narrow (solid line) and wide (dashed line) region, compared with the unperturbed Maxwellian distribution (dotted line).

derived from the turbulent field in Figure 12c is relatively small amplitude. The Fokker-Planck simulation in Figure 15a shows the excitation of relatively weak suprathermal tails. For the wider (1 km) region in Figure 15b, a small fraction of electrons reaches a velocity of about 2×10^6 m/s, corresponding to about 11 eV energy. The turbulence would likely give rise to optical emissions but not to significant ionization of the neutral gas. At the lower altitude (cf. Figures 11d–11f) the weak wave turbulence gives rise to a narrow wave spectrum and to diffusion coefficient which only has two narrow peaks (cf. Figure 12d), and for this case no significant suprathermal tails are created in the electron distribution function (not shown). The injected amplitude of $E_{EM} = 0.2$ V/m may be regarded as a lower bound for inducing artificial ionospheric turbulence strong enough to efficiently accelerate electrons. Thermal expansion near the O mode Airy maxima [*Erukhimov et al.*, 1997] could here lead to periodic patterns extending along the magnetic field lines.

6. Conclusions

We have carried out an extensive investigation of the propagation and nonlinear interaction between large-amplitude EM waves and the ionospheric plasma in the magnetic equatorial region. The equatorial region has unique features that distinguish it from the midlatitude and auroral regions. Since the magnetic field is horizontal, O mode waves injected vertically and within the Spitze region will be linearly polarized near the critical layer with the wave electric field parallel to the magnetic field. This leads to the excitation of Langmuir turbulence in a several kilometers wide region below the critical layer and efficient electron acceleration along the magnetic field lines due to resonant interactions with the turbulent Langmuir waves. Simulations of the nonlinear evolution of the instability and of the interaction between the electrons and the turbulent electric field show that suprathermal tails of electrons are created by the turbulence and can reach

energies of several tens to a few hundreds of eV, which is far above the thresholds for optical emissions and ionization of the neutral gas. The suprathermal electrons could also excite shear Alfvén waves such as those observed in recent experiments at the UCLA LAPD device [*Van Compernolle et al.*, 2006; *Wang et al.*, 2016].

Appendix A: Nonlinear Dispersion Relation for the PDI and OTSI

The instability for Langmuir turbulence is estimated using the Langmuir wave equation

$$\left[\frac{\partial^2}{\partial t^2} + v_e \frac{\partial}{\partial t} - 3v_{Te}^2 \frac{\partial^2}{\partial x^2} + \omega_{pe}^2 \left(1 + \frac{n_s}{n_0}\right)\right] E_x = 0 \tag{A1}$$

coupled with the ion acoustic wave equation

$$\left(\frac{\partial^2}{\partial t^2} + 2v_i \frac{\partial}{\partial t} - C_s^2 \frac{\partial^2}{\partial x^2}\right) n_s = \frac{\epsilon_0}{2m_i} \frac{\partial^2 \langle E_x^2 \rangle}{\partial x^2} \quad, \tag{A2}$$

where the angular brackets denote averaging over a HF wave period. By using a four-wave interaction model, we do the Fourier decomposition $E_x = (1/2)e^{-i\omega_0 t}\left(\hat{E}_0 + \hat{E}_+ e^{-i\omega_1 t + ik_1 x} + \hat{E}_- e^{i\omega_1^* t - ik_1 x}\right) +$ complex conjugate and $n_s = (1/2)\hat{n}_s e^{-i\omega_1 t + ik_1 x} +$ complex conjugate, where ω_1 and k_1 is the perturbation frequency and wave number, respectively, and the asterisk denotes complex conjugation taking into account that ω_1 is complex valued. Here the complex amplitude $\hat{E}_0$ represents the large-amplitude pump wave, $\hat{E}_+$ and $\hat{E}_-$ represents the small-amplitude HF sidebands ($|\hat{E}_0| \gg |\hat{E}_+|, |\hat{E}_+|$), and $\hat{n}_s$ represents the small-amplitude ion density fluctuations ($n_0 \gg |\hat{n}_s|$). Separating different Fourier components, we find from equation (A1)

$$\left[-(\omega_0 + \omega_1)^2 - iv_e(\omega_0 + \omega_1) + 3v_{Te}^2 k_1^2 + \omega_{pe}^2\right]\hat{E}_+ + \omega_{pe}^2 \hat{E}_0 \frac{\hat{n}_s}{n_0} = 0 \quad, \tag{A3}$$

$$\left[-(-\omega_0 + \omega_1)^2 + iv_e(-\omega_0 + \omega_1) + 3v_{Te}^2 k_1^2 + \omega_{pe}^2\right]\hat{E}_-^* + \omega_{pe}^2 \hat{E}_0^* \frac{\hat{n}_s}{n_0} = 0 \quad, \tag{A4}$$

and from equation (A2)

$$\left(-\omega_1^2 - 2iv_i\omega_1 + C_s^2 k_1^2\right)\hat{n}_s = -\frac{\epsilon_0 k_1^2}{4m_i}\left(\hat{E}_0^* \hat{E}_+ + \hat{E}_0 \hat{E}_-^*\right) \quad. \tag{A5}$$

Solving for $\hat{E}_+$ and $\hat{E}_-^*$ in equations (A3) and (A4) and inserting into equation (A5) with $\hat{E}_0^* \hat{E}_0 = \left|\hat{E}_0\right|^2 \equiv E_0^2$ gives the nonlinear dispersion relation (6) for the OTSI and PDI.

References

Eliasson, B., and L. Stenflo (2008), Full-scale simulation study of the initial stage of ionospheric turbulence, *J. Geophys. Res.*, *113*, A02305, doi:10.1029/2007JA012837.

Eliasson, B., X. Shao, G. Milikh, E. V. Mishin, and K. Papadopoulos (2012), Numerical modeling of artificial ionospheric layers driven by high-power HF-heating, *J. Geophys. Res.*, *117*, A10321, doi:10.1029/2012JA018105.

Eliasson, B., G. Milikh, X. Shao, E. V. Mishin, and K. Papadopoulos (2015), Incidence angle dependence of Langmuir turbulence and artificial ionospheric layers driven by high-power HF-heating, *J. Plasma Phys.*, *81*, 415810201, doi:10.1017/S0022377814000968.

Erukhimov, L. M., N. A. Mityakov, and B. Thidé (1997), On the excitation of the ionosphere by high-power radio waves in the geomagnetic equator region, *Radiophys. Quantum Electron.*, *40*(1–2), 165–173.

Freund, H. P., and K. Papadopoulos (1980), Oscillating two-stream and parametric decay instabilities in a weakly magnetized plasma, *Phys. Fluids*, *23*(1), 139–146.

Gumerov, N. A., A. V. Karavaev, A. S. Sharma, X. Shao, and K. D. Papadopoulos (2011), Efficient spectral and pseudospectral algorithms for 3D simulations of whistler-mode waves in a plasma, *J. Comput. Phys.*, *230*(7), 2605–2619, doi:10.1016/j.jcp.2010.12.038.

Gurevich, A. V. (1978), *Nonlinear phenomena in the ionosphere*, Springer, New York.

Ivanov, A. A., T. K. Soboleva, and P. N. Yushmanov (1975), Three-dimensional quasi-linear relaxation, *Sov. Phys. JETP*, *42*(6), 1027–1035.

Krall, N. A., and A. W. Trivelpiece (1986), *Principles of Plasma Physics*, San Francisco Press, Inc., San Francisco, Calif.

Mishin, E., and T. Pedersen (2011), Ionizing wave via high-power HF acceleration, *Geophys. Res. Lett.*, *38*, L01105, doi:10.1029/2010GL046045.

Mjølhus, E. (1990), On linear mode conversion in a magnetized plasma, *Radio Sci.*, *25*, 1321–1339, doi:10.1029/RS025i006p01321.

Mjølhus, E., A. Hanssen, and D. F. DuBois (1995), Radiation from electromagnetically driven Langmuir turbulence, *J. Geophys. Res.*, *100*, 17,527–17,541, doi:10.1029/95JA01158.

Mjølhus, E., E. Helmersen, and D. F. DuBois (2003), Geometric aspects of HF driven Langmuir turbulence in the ionosphere, *Nonlinear Processes Geophys.*, *10*, 151–177, doi:10.5194/npg-10-151-2003.

Moore, R. C. (2007), ELF/VLF wave generation by modulated heating of the auroral electrojet, PhD thesis, Stanford Univ., Stanford, Calif.

Papadopoulos, K. (2015), Ionspheric modifcations using mobile, high power HF transmitters based on TPM technology, paper presented at 2015 IEEE International Conference on Plasma Science (ICOPS), 24–28 May, Antalya, Turkey.

Papadopoulos, K., M. L. Goldstein, and R. A. Smith (1974), Stabilization of electron streams in type III solar radio bursts, *Astrophys. J.*, *190*, 175–185.

Papadopoulos, K., C. L. Chang, P. Vitello, and A. Drobot (1990), On the efficiency of ionospheric ELF generation, *Radio Sci.*, *25*, 1311–1320, doi:10.1029/RS025i006p01311.

Papadopoulos, K., T. Wallace, G. M. Milikh, W. Peter, and M. McCarrick (2005), The magnetic response of the ionosphere to pulsed HF heating, *Geophys. Res. Lett.*, *32*, L13101, doi:10.1029/2005GL023185.

Payne, J. A., U. S. Inan, F. R. Foust, T. W. Chevalier, and T. F. Bell (2007), HF modulated ionospheric currents, *Geophys. Res. Lett.*, *34*, L23101, doi:10.1029/2007GL031724.

Pedersen, T., B. Gustavsson, E. Mishin, E. MacKenzie, H. C. Carlson, M. Starks, and T. Mills (2009), Optical ring formation and ionization production in high-power HF heating experiments at HAARP, *Geophys. Res. Lett.*, *36*, L18107, doi:10.1029/2009GL040047.

Pedersen, T., B. Gustavsson, E. Mishin, E. Kendall, T. Mills, H. C. Carlson, and A. L. Snyder (2010), Creation of artificial ionospheric layers using high-power HF waves, *Geophys. Res. Lett.*, *37*, L02106, doi:10.1029/2009GL041895.

Rees, M. H. (1989), *Physics and Chemistry of the Upper Atmosphere*, Cambridge Univ. Press, Cambridge, U. K.

Rietveld, M. T., R. Barr, H. Kopka, E. Nielson, P. Stubbe, and R. L. Dowden (1984), Ionospheric heater beam scanning: A new technique for ELF studies of the auroral ionosphere, *Radio Sci.*, *19*, 1069–1077, doi:10.1029/RS019i004p01069.

Rietveld, M. T., H.-P. Mauelshagen, P. Stubbe, H. Kopka, and E. Nielsen (1987), The characteristics of ionospheric heating-produced ELF/VLF waves over 32 hours, *J. Geophys. Res.*, *92*, 8707–8722, doi:10.1029/JA092iA08p08707.

Rietveld, M. T., P. Stubbe, and H. Kopka (1989), On the frequency dependence of ELF/VLF waves produced by modulated ionospheric heating, *Radio Sci.*, *24*, 270–278, doi:10.1029/RS024i003p00270.

Russell, D., D. F. DuBois, and H. A. Rose (1988), Nucleation in two-dimensional Langmuir turbulence, *Phys. Rev. Lett.*, *60*(7), 581–584.

Sagdeev, R. Z., and A. Galeev (1969), *Nonlinear Plasma Theory*, Benjamin, New York.

Stenflo, L. (1985), Parametric excitation of collisional modes in the high-latitude ionosphere, *J. Geophys. Res.*, *90*, 5355–5356, doi:10.1029/JA090iA06p05355.

Stix, T. H. (1992), *Waves in Plasmas*, Am. Inst. of Phys., New York.

Thornhill, S. G., and D. ter Haar (1978), Langmuir turbulence and modulational instability, *Phys. Rep.*, *43*(2), 43–99, doi:10.1016/0370-1573(78)90142-4.

Tsung, F. S., G. J. Morales, and J. Tonge (2007), Alfvénic phenomena triggered by resonant absorption of an O-mode pulse, *Phys. Plasmas*, *14*, 042101.

Van Compernolle, B., W. Gekelman, and P. Pribyl (2006), Generation of suprathermal electrons and Alfvén waves by a high power pulse at the electron plasma frequency, *Phys. Plasmas*, *13*, 092112.

Vedenov, A. A., E. P. Velikhov, and R. Z. Sagdeev (1961), Nonlinear oscillations of rarified plasma, *Nucl. Fusion*, *1*, 82–100.

Wang, Y., W. Gekelman, P. Pribyl, B. Van Compernolle, and K. Papadopoulos (2016), Generation of kinetic shear Alfvén waves by repetitive electron heating, *J. Geophys. Res. Space Physics*, *121*, 567–577, doi:10.1002/2015JA022078.

Whitham, G. B. (1974), *Linear and Nonlinear Waves*, John Wiley, New York.